atoms

MDPI

Article

Modelling of X-Ray Spectra Originating from the He- and Li-like Ni Ions for Plasma Electron Temperature Diagnostics Purposes

Karol Kozioł *, Andrzej Brosławski and Jacek Rzadkiewicz

Narodowe Centrum Badań Jądrowych (NCBJ), Andrzeja Sołtana 7, 05-400 Otwock-Świerk, Poland; andrzej.broslawski@ncbj.gov.pl (A.B.); jacek.rzadkiewicz@ncbj.gov.pl (J.R.)
* Correspondence: karol.koziol@ncbj.gov.pl

Abstract: The multi-configurational Dirac–Hartree–Fock method has been used to examine the electron correlation effect on wavelengths and transition rates for $L \rightarrow K$ transitions occurring in He- and Li-like nickel ions. The collisional-radiative modelling approach has been used to simulate the X-ray spectra, in a 1.585–1.620 Å wavelength range, originating from the He-like nickel ions and their dielectronic Li-, Be-, and B-like satellites for various electron temperature values in the 2 keV to 8 keV range. The presented results may be useful in improving the plasma electron temperature diagnostics based on nickel spectra.

Keywords: atomic spectra; electron correlation; collisional-radiative modelling

1. Introduction

Nickel is among the most cosmically abundant heavy elements and has been observed in various astrophysical bodies. Nickel spectra are of great interest in astrophysics studies and they can be used to estimate quantities of interest such as the redshift, temperature, abundance, and the velocity of the emitting gas [1,2]. Nickel spectra are present in large fusion reactors, such as the Joint European Torus (JET) [3–5], the Experimental Advanced Superconducting Tokamak (EAST) [6], and the Wendelstein 7-X stellarator [7]. High-resolution X-ray spectroscopy of He-like ions has been proven to be a very useful tool for determining various parameters in tokamak plasma devices, including ion and electron temperature, toroidal rotation velocity, metallic impurity concentrations and effective charge Z_{eff} [3,8–12]. In particular, measurements of the X-ray spectra of the He-like Ni ions (Ni^{26+}) and their dielectronic satellites (Ni^{25+}, Ni^{24+}, and Ni^{23+}) play a pivotal role in the determination of electron and ion temperature and toroidal rotation for the JET plasmas (KX1 diagnostic) [10–12]. At JET, the high-resolution X-ray diagnostic of the ion temperature relies on the thermal Doppler broadening of the helium-like nickel resonance w line at 1.5856 Å (see Table 1 for the line labeling used in this paper). Therefore, the spectra of He-like and Li-like Ni ions have been an object of interest in many theoretical studies [1,3,13–20].

The dielectronic satellites of Ni^{25+} overlap with the resonance line of Ni^{26+}, making it crucial to reliably reconstruct the structure of these satellites. This is especially important in the cases when plasma rotation is high, which may result in an additional broadening of the resonance line. In our previous paper [4], we investigated potential causes of the additional broadening of the resonance line due to the effect of overlapping of the dielectronic satellites with the resonance line of Ni^{26+} and the effect of toroidal plasma rotation shear. During the study, a couple of theoretical issues arose. The first one is an effect of electron correlation on the determination of line ratios. The second one is the calibration of the collisional-radiative modelling (CRM) simulations. Both of them are investigated in the present work.

check for updates

Academic Editor: Chihiro Suzuki

Received: 18 December 2024
Revised: 27 January 2025
Accepted: 7 February 2025
Published: 9 February 2025

Citation: Kozioł, K.; Brosławski, A.; Rzadkiewicz, J. Modelling of X-Ray Spectra Originating from the He- and Li-like Ni Ions for Plasma Electron Temperature Diagnostics Purposes. *Atoms* **2025**, *13*, 18. https://doi.org/10.3390/atoms13020018

Copyright: © 2025 by the authors. Licensee MDPI, Basel, Switzerland. This article is an open access article distributed under the terms and conditions of the Creative Commons Attribution (CC BY) license (https://creativecommons.org/licenses/by/4.0/).

Table 1. Nomenclature of $L \rightarrow K$ transitions in He-, Li-, and Be-like ions, according to refs. [3,21]. Level labeling in both LSJ and jj coupling schemes are presented.

Line	Initial (Upper) State		Final (Lower) State	
	LSJ	**jj**	**LSJ**	**jj**
He-like ions				
w	$1s\,2p\ ^1P_1$	$[1s_{1/2}\,2p_{3/2}]_1$	$1s^2\ ^1S_0$	$[1s^2_{1/2}]_0$
x	$1s\,2p\ ^3P_2$	$[1s_{1/2}\,2p_{3/2}]_2$	$1s^2\ ^1S_0$	$[1s^2_{1/2}]_0$
y	$1s\,2p\ ^3P_1$	$[1s_{1/2}\,2p_{1/2}]_1$	$1s^2\ ^1S_0$	$[1s^2_{1/2}]_0$
z	$1s\,2s\ ^3S_1$	$[1s_{1/2}\,2s_{1/2}]_1$	$1s^2\ ^1S_0$	$[1s^2_{1/2}]_0$
Li-like ions				
a	$1s\,2p^2\ ^2P_{3/2}$	$[1s_{1/2}\,(2p^2_{3/2})_2]_{3/2}$	$1s^2\,2p\ ^2P_{3/2}$	$[1s^2_{1/2}\,2p_{3/2}]_{3/2}$
b	$1s\,2p^2\ ^2P_{3/2}$	$[1s_{1/2}\,(2p^2_{3/2})_2]_{3/2}$	$1s^2\,2p\ ^2P_{1/2}$	$[1s^2_{1/2}\,2p_{1/2}]_{1/2}$
c	$1s\,2p^2\ ^2P_{1/2}$	$[(1s_{1/2}\,2p_{1/2})_1\,2p_{3/2}]_{1/2}$	$1s^2\,2p\ ^2P_{3/2}$	$[1s^2_{1/2}\,2p_{3/2}]_{3/2}$
d	$1s\,2p^2\ ^2P_{1/2}$	$[(1s_{1/2}\,2p_{1/2})_1\,2p_{3/2}]_{1/2}$	$1s^2\,2p\ ^2P_{1/2}$	$[1s^2_{1/2}\,2p_{1/2}]_{1/2}$
e	$1s\,2p^2\ ^4P_{5/2}$	$[(1s_{1/2}\,2p_{1/2})_1\,2p_{3/2}]_{5/2}$	$1s^2\,2p\ ^2P_{3/2}$	$[1s^2_{1/2}\,2p_{3/2}]_{3/2}$
f	$1s\,2p^2\ ^4P_{3/2}$	$[(1s_{1/2}\,2p_{1/2})_1\,2p_{3/2}]_{3/2}$	$1s^2\,2p\ ^2P_{3/2}$	$[1s^2_{1/2}\,2p_{3/2}]_{3/2}$
g	$1s\,2p^2\ ^4P_{3/2}$	$[(1s_{1/2}\,2p_{1/2})_1\,2p_{3/2}]_{3/2}$	$1s^2\,2p\ ^2P_{1/2}$	$[1s^2_{1/2}\,2p_{1/2}]_{1/2}$
h	$1s\,2p^2\ ^4P_{1/2}$	$[1s_{1/2}\,(2p^2_{1/2})_0]_{1/2}$	$1s^2\,2p\ ^2P_{3/2}$	$[1s^2_{1/2}\,2p_{3/2}]_{3/2}$
i	$1s\,2p^2\ ^4P_{1/2}$	$[1s_{1/2}\,(2p^2_{1/2})_0]_{1/2}$	$1s^2\,2p\ ^2P_{1/2}$	$[1s^2_{1/2}\,2p_{1/2}]_{1/2}$
j	$1s\,2p^2\ ^2D_{5/2}$	$[1s_{1/2}\,(2p^2_{3/2})_2]_{5/2}$	$1s^2\,2p\ ^2P_{3/2}$	$[1s^2_{1/2}\,2p_{3/2}]_{3/2}$
k	$1s\,2p^2\ ^2D_{3/2}$	$[(1s_{1/2}\,2p_{1/2})_0\,2p_{3/2}]_{3/2}$	$1s^2\,2p\ ^2P_{1/2}$	$[1s^2_{1/2}\,2p_{1/2}]_{1/2}$
l	$1s\,2p^2\ ^2D_{3/2}$	$[(1s_{1/2}\,2p_{1/2})_0\,2p_{3/2}]_{3/2}$	$1s^2\,2p\ ^2P_{3/2}$	$[1s^2_{1/2}\,2p_{3/2}]_{3/2}$
m	$1s\,2p^2\ ^2S_{1/2}$	$[1s_{1/2}\,(2p^2_{3/2})_0]_{1/2}$	$1s^2\,2p\ ^2P_{3/2}$	$[1s^2_{1/2}\,2p_{3/2}]_{3/2}$
n	$1s\,2p^2\ ^2S_{1/2}$	$[1s_{1/2}\,(2p^2_{3/2})_0]_{1/2}$	$1s^2\,2p\ ^2P_{1/2}$	$[1s^2_{1/2}\,2p_{1/2}]_{1/2}$
o	$1s\,2s^2\ ^2S_{1/2}$	$[1s_{1/2}\,2s^2_{1/2}]_{1/2}$	$1s^2\,2p\ ^2P_{3/2}$	$[1s^2_{1/2}\,2p_{3/2}]_{3/2}$
p	$1s\,2s^2\ ^2S_{1/2}$	$[1s_{1/2}\,2s^2_{1/2}]_{1/2}$	$1s^2\,2p\ ^2P_{1/2}$	$[1s^2_{1/2}\,2p_{1/2}]_{1/2}$
q	$(1s\,2p\ ^1P)\,2s\ ^2P_{3/2}$	$[(1s_{1/2}\,2s_{1/2})_1\,2p_{3/2}]_{3/2}$	$1s^2\,2s\ ^2S_{1/2}$	$[1s^2_{1/2}\,2s_{1/2}]_{1/2}$
r	$(1s\,2p\ ^1P)\,2s\ ^2P_{1/2}$	$[(1s_{1/2}\,2s_{1/2})_0\,2p_{1/2}]_{1/2}$	$1s^2\,2s\ ^2S_{1/2}$	$[1s^2_{1/2}\,2s_{1/2}]_{1/2}$
s	$(1s\,2p\ ^3P)\,2s\ ^2P_{3/2}$	$[(1s_{1/2}\,2s_{1/2})_0\,2p_{3/2}]_{3/2}$	$1s^2\,2s\ ^2S_{1/2}$	$[1s^2_{1/2}\,2s_{1/2}]_{1/2}$
t	$(1s\,2p\ ^3P)\,2s\ ^2P_{1/2}$	$[(1s_{1/2}\,2s_{1/2})_1\,2p_{3/2}]_{1/2}$	$1s^2\,2s\ ^2S_{1/2}$	$[1s^2_{1/2}\,2s_{1/2}]_{1/2}$
u	$(1s\,2p)\,2s\ ^4P_{3/2}$	$[(1s_{1/2}\,2s_{1/2})_1\,2p_{1/2}]_{3/2}$	$1s^2\,2s\ ^2S_{1/2}$	$[1s^2_{1/2}\,2s_{1/2}]_{1/2}$
v	$(1s\,2p)\,2s\ ^4P_{1/2}$	$[(1s_{1/2}\,2s_{1/2})_1\,2p_{1/2}]_{1/2}$	$1s^2\,2s\ ^2S_{1/2}$	$[1s^2_{1/2}\,2s_{1/2}]_{1/2}$
Be-like ions				
β	$1s\,2s^2\,2p\ ^1P_1$	$[1s_{1/2}\,2s^2_{1/2}\,2p_{3/2}]_1$	$1s^2\,2s^2\ ^1S_0$	$[1s^2_{1/2}\,2s^2_{1/2}]_0$

2. Electron Correlation Effect

The multi-configurational Dirac–Hartree–Fock (MCDHF) method, as implemented in the GRASP2018 code [22], has been applied to study the effects of electron correlation on the wavelengths and transition rates for $L \rightarrow K$ transitions in He- and Li-like Ni ions. The methodology for the MCDHF calculations used in this study aligns with approaches described in previous works (e.g., [23]). The effective Hamiltonian for an N-electron system is given by

$$H = \sum_{i=1}^{N} h_D(i) + \sum_{j>i=1}^{N} C_{ij}, \tag{1}$$

where $h_D(i)$ represents the Dirac operator for the ith electron, and C_{ij} accounts for electron–electron interactions. These interactions typically include the Coulomb interaction operator

and the transverse Breit operator. The atomic state function (ASF) with total angular momentum J and parity p is expressed as

$$\Psi_s(J^p) = \sum_m c_m(s)\Phi(\gamma_m J^p), \tag{2}$$

where $\Phi(\gamma_m J^p)$ is the configuration state function (CSF), $c_m(s)$ is the configuration mixing coefficient for state s, and γ_m contains the information needed to uniquely define a CSF. The CSFs themselves are linear combinations of N-electron Slater determinants, which are antisymmetrized products of 4-component Dirac orbital spinors. In the present calculations, the initial and final states of the transitions were optimized independently, and transition rate calculations were performed using the biorthonormal transformation method [24], thereby accounting for the orbital relaxation effect. The accuracy of the wavefunction depends on the CSFs included in its expansion [25,26], which can be enhanced by extending the CSF set. This is achieved by generating CSFs through substitutions from the occupied orbitals in the reference CSFs to unoccupied (virtual) orbitals within the active orbital set (Active Space, AS). The relativistic configuration interaction (CI) method is employed to capture the dominant electron correlation effects, thereby improving the energy levels and transition strengths. In the CI approach, the selection of a proper CSF basis for virtual excited states is crucial. This is accomplished by systematically extending the active space of orbitals and monitoring the convergence of the self-consistent calculations.

The multireference set, MR, for a given initial or final state of transition of interest contains CSFs related to the electronic configuration presented in Table 1. To construct substitution sets, all single (S) and double (D) substitutions from the 1s, 2s, and 2p orbitals to the active spaces of virtual orbitals were employed. The virtual orbital sets used were AS1 = {2s,2p}, AS2 = AS1 + {3s,3p,3d}, AS3 = AS2 + {4s,4p,4d,4f}, AS4 = AS3 + {5s,5p,5d,5f,5g}, AS5 = AS4 + {6s,6p,6d,6f,6g,6h}. So, for example, for an MR of a single $[1s^2_{1/2}]_0$ state, the AS1 contains five CSFs generated by substitution rules described above: $[1s^2_{1/2}]_0$, $[1s_{1/2}2s_{1/2}]_0$, $[2s^2_{1/2}]_0$, $[2p^2_{1/2}]_0$, and $[2p^2_{3/2}]_0$. The numbers of CSFs used in active spaces in the present work are listed in Table 2.

Table 2. Number of CSFs used for given active spaces considered for upper and lower states (one electronic configuration or group of configurations) of $L \rightarrow K$ transitions occurring in the He- and Li-like Ni ions.

Active	**Number of CSFs**				
Space	$[1s^2_{1/2}]_0$	$[1s_{1/2}2s_{1/2}]_1$	$[1s_{1/2}2p_{3/2}]_{1,2}$	$[1s^2 2(s,p)^1]_{1/2,3/2}$	$[1s^1 2(s,p)^2]_{1/2,3/2,5/2}$
MR	1	1	3	3	16
AS1	5	2	6	14	34
AS2	14	13	32	70	380
AS3	30	39	96	194	1459
AS4	53	82	196	410	3630
AS5	83	142	332	742	7237

Figures 1 and 2 present the MCDHF-CI convergence of energy of the considered lines, in the form of an E(ASn)–E(MR) vs. ASn plot. As one can see from these figures, the AS5 stage seems to be enough to achieve convergence of high MCDHF-CI calculations for lines of He-like (Figure 1) and slightly weaker convergence for lines of Li-like Ni ions (Figure 2). Figures 3 and 4 present the MCDHF-CI convergence of energy of the considered lines, in the form of [A(ASn) − A(MR)]/A(MR) vs. ASn plot. Usually, the difference between transition rates calculated for different ASs is in order of a few percent. However, for the weakest transitions, such a difference is much larger, because, in this case, even a small

difference in the wavefunction caused by CI may result in a large change in the matrix element of a dipole operator.

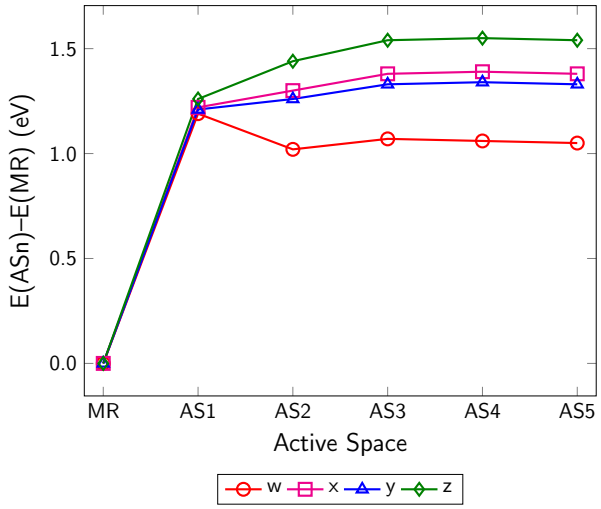

Figure 1. Convergence of CI calculations for transition energies in He-like Ni.

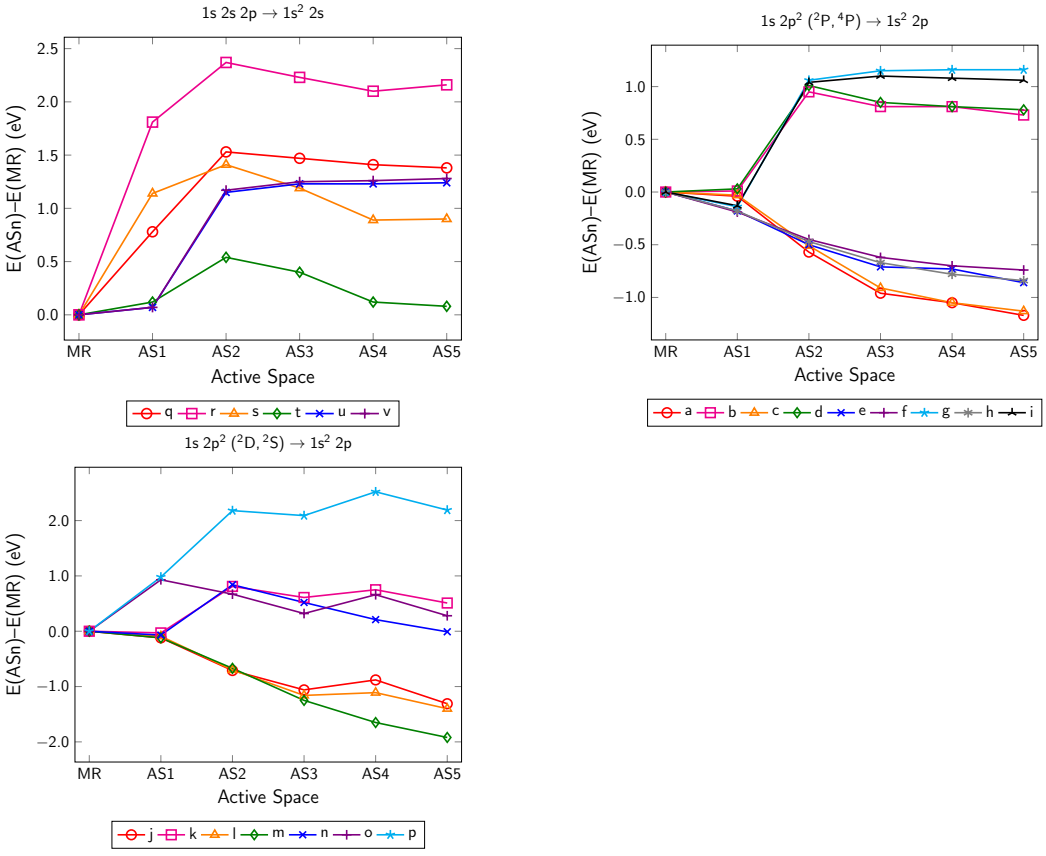

Figure 2. Convergence of CI calculations for transition energies in Li-like Ni.

Tables 3–6 present the wavelengths and transition rates of considered $L \rightarrow K$ lines, calculated using the GRASP2018 code as well as the FAC code [27] and compared to the reference values from the NIST Atomic Spectra Database [28]. The data from Bombarda et al.'s work [3] are also presented, because they are the base for internal subroutines of KX1 diagnostics of JET. The MR and GRASP MCDHF-CI approaches are as described above. The FAC-CI values are calculated by an in-build `atomic_data` subroutine (the FAC input as a Python file is presented in Figure 5) that generates atomic data suitable to following CRM simulations and automatically makes the CI between configurations of interest. The

equivalent CI AS for Ni^{26+} contains configurations with D excitations to orbitals with $n \leq 3$ and $l \leq 2$ and S excitations to orbitals with $n \leq 9$ and $l \leq 8$. The equivalent CI AS for Ni^{25+} contains configurations with D excitations to orbitals with $n \leq 3$ and $l \leq 2$ and S excitations to orbitals with $n \leq 7$ and $l \leq 6$.

Table 3. Wavelengths (Å) for $L \rightarrow K$ transitions in He-like Ni ions.

Line	MCDHF-CI		FAC				Bombarda et al. [3]
	MR	CI	MR	CI	NIST	Exp.	Theo.
w	1.58862	1.58840	1.58852	1.58848	1.5884	1.5886	1.5856
x	1.59259	1.59231	1.59256	1.59241	1.5923	1.5925	1.5897
y	1.59683	1.59656	1.59679	1.59664	1.5966	1.5966	1.5941
z	1.60392	1.60360	1.60386	1.60363	1.6036	1.6038	1.6010

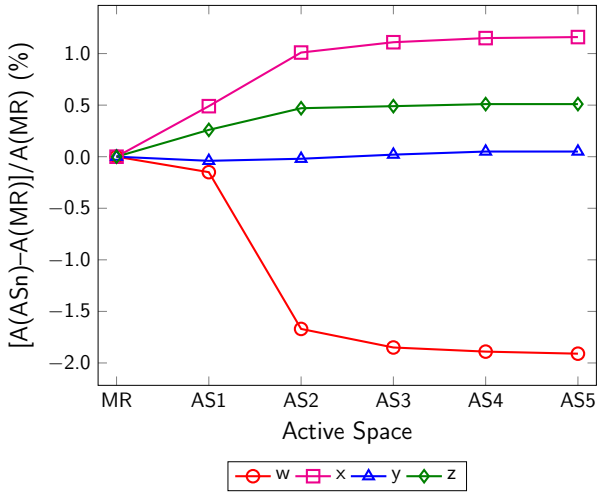

Figure 3. Convergence of CI calculations for transition rates in He-like Ni.

As one can see from Tables 3–6, the electron correlation effect on wavelengths and transition rates (except for the weakest lines) of the considered lines is not very large; however, it should be taken into account if high accuracy of simulations is required. In the case of line ratios, the effects of electron correlation mostly cancel each other out, but not in all cases. For example, the x/w ratio calculated at the AS5 level of theory is higher by 2.9% than such a ratio calculated at MR level of theory. Similar change for the y/w ratio is 2.1%. For the t/w and q/w ratios, the difference between AS5 and MR levels of theory are much smaller and they are at 0.1% and 0.2%, respectively. There are some differences between MCDHF-CI and FAC-CI values used for CRM simulations. The difference between MCDHF-CI and FAC-CI values for the y/w, x/w, q/w, and t/w ratios are 7.6%, 2.5%, 1.1%, 0.4%, respectively.

Table 4. Transition rates (A, length gauge, s^{-1}) and weighted oscillator strengths (gf, length gauge) for $L \rightarrow K$ transitions in He-like Ni ions.

Line	MCDHF-CI				FAC					
	MR		CI		MR		CI		NIST	
	A	gf	A	gf	A	gf	A	gf	A	gf
w	6.14×10^{14}	6.97×10^{-1}	6.02×10^{14}	6.83×10^{-1}	6.13×10^{14}	6.95×10^{-1}	6.21×10^{14}	7.05×10^{-1}	6.02×10^{14}	6.83×10^{-1}
x	1.18×10^{10}	2.25×10^{-5}	1.19×10^{10}	2.27×10^{-5}	1.18×10^{10}	2.24×10^{-5}	1.20×10^{10}	2.29×10^{-5}	1.22×10^{10}	2.32×10^{-6}
y	7.71×10^{13}	8.84×10^{-2}	7.72×10^{13}	8.85×10^{-2}	7.56×10^{13}	8.67×10^{-2}	7.40×10^{13}	8.49×10^{-2}	7.70×10^{13}	8.83×10^{-2}
z	4.37×10^{8}	5.04×10^{-7}	4.38×10^{8}	5.06×10^{-7}	4.22×10^{8}	4.88×10^{-7}	4.22×10^{8}	4.88×10^{-7}	4.52×10^{8}	5.23×10^{-7}

Table 5. Wavelengths (Å) for $L \rightarrow K$ transitions in Li-like Ni ions.

Line	MCDHF-CI		FAC			Bombarda et al. [3]	
	MR	CI	MR	CI	NIST	Exp.	Theo.
a	1.59786	1.59810	1.59787	1.59789	1.5978		1.5950
b	1.59334	1.59319	1.59336	1.59337	1.5932		1.5899
c	1.60317	1.60340	1.60317	1.60319	1.6029		1.6004
d	1.59862	1.59846	1.59863	1.59865	1.5984		1.5953
e	1.60714	1.60732	1.60717	1.60716	1.6069		1.6046
f	1.60870	1.60886	1.60853	1.60873	1.6084		1.6066
g	1.60412	1.60388	1.60417	1.60415	1.6038		
h	1.61124	1.61142	1.61127	1.61126	1.6108		
i	1.60665	1.60643	1.60669	1.60667	1.6062		1.6040
j	1.60100	1.60127	1.60104	1.60104	1.6010	1.6011	1.5983
k	1.59849	1.59838	1.59854	1.59854	1.5984	1.5987	1.5956
l	1.60303	1.60332	1.60308	1.60308	1.6029		1.6007
m	1.59351	1.59390	1.59361	1.59363	1.5940		1.5910
n	1.58902	1.58902	1.58912	1.58914	1.5891		1.5859
o	1.62789	1.62783	1.62768	1.62768	1.6274		1.6252
p	1.62320	1.62273	1.62300	1.62300	1.6227		1.6199
q	1.59724	1.59696	1.59715	1.59716	1.5970	1.5972	1.5941
r	1.60021	1.59977	1.59990	1.59992	1.5997	1.5999	1.5973
s	1.59318	1.59300	1.59302	1.59303	1.5931		1.5905
t	1.59379	1.59377	1.59385	1.59385	1.5938	1.5940	1.5911
u	1.60810	1.60784	1.60810	1.60808	1.6077		1.6052
v	1.60911	1.60884	1.60911	1.60910	1.6087		1.6066

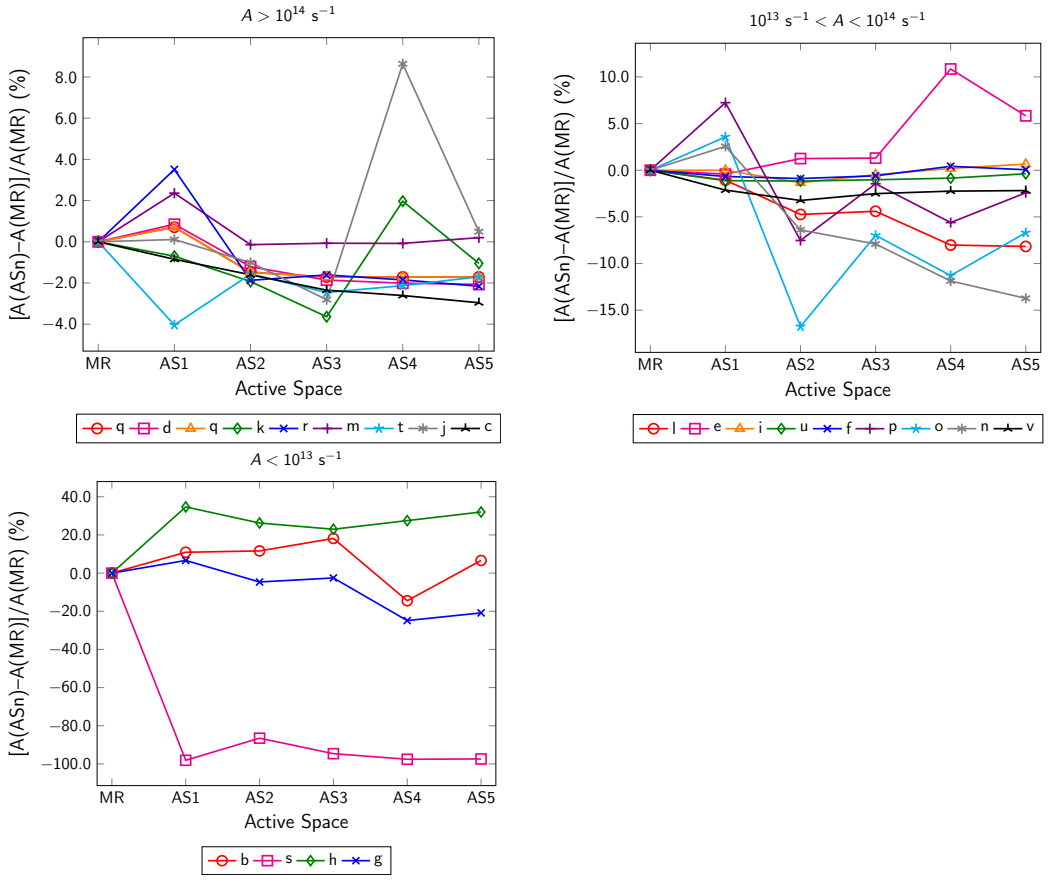

Figure 4. Convergence of CI calculations for transition rates in Li-like Ni.

Table 6. Transition rates (A, length gauge, s^{-1}) and weighted oscillator strengths (gf, length gauge) for $L \rightarrow K$ transitions in Li-like Ni ions.

Line	MCDHF-CI				FAC						Bombarda
	MR		CI		MR		CI		NIST		et al. [3] (Theo.)
	A	gf	A	gf	A	gf	A	gf	A	gf	A
a	7.99×10^{14}	1.22	7.92×10^{14}	1.21	7.91×10^{14}	1.21	8.03×10^{14}	1.23	8.1×10^{14}	1.24	8.35×10^{14}
b	5.82×10^{12}	8.86×10^{-3}	6.20×10^{12}	9.44×10^{-3}	6.66×10^{12}	1.01×10^{-2}	6.20×10^{12}	9.44×10^{-3}			1.17×10^{13}
c	2.12×10^{14}	1.64×10^{-1}	2.06×10^{14}	1.59×10^{-1}	2.09×10^{14}	1.61×10^{-1}	2.08×10^{14}	1.60×10^{-1}	2.1×10^{14}	1.6×10^{-1}	2.01×10^{14}
d	7.15×10^{14}	5.48×10^{-1}	7.00×10^{14}	5.36×10^{-1}	7.08×10^{14}	5.43×10^{-1}	7.14×10^{14}	5.47×10^{-1}	7.3×10^{14}	5.6×10^{-1}	7.32×10^{14}
e	6.64×10^{13}	1.54×10^{-1}	7.02×10^{13}	1.63×10^{-1}	6.47×10^{13}	1.50×10^{-1}	6.49×10^{13}	1.51×10^{-1}			6.65×10^{13}
f	1.91×10^{13}	2.97×10^{-2}	1.92×10^{13}	2.97×10^{-2}	7.67×10^{7}	1.19×10^{-7}	1.82×10^{13}	2.83×10^{-2}			1.48×10^{13}
g	8.93×10^{10}	1.38×10^{-4}	7.07×10^{10}	1.09×10^{-4}	8.73×10^{10}	1.35×10^{-4}	6.97×10^{10}	1.08×10^{-4}			
h	1.24×10^{11}	9.63×10^{-5}	1.63×10^{11}	1.27×10^{-4}	1.43×10^{11}	1.11×10^{-4}	9.78×10^{10}	7.61×10^{-5}			
i	4.63×10^{13}	3.58×10^{-2}	4.66×10^{13}	3.61×10^{-2}	4.55×10^{13}	3.52×10^{-2}	4.42×10^{13}	3.42×10^{-2}			4.28×10^{13}
j	2.70×10^{14}	6.22×10^{-1}	2.71×10^{14}	6.25×10^{-1}	2.61×10^{14}	6.03×10^{-1}	2.68×10^{14}	6.18×10^{-1}	2.7×10^{14}	6.4×10^{-1}	2.74×10^{14}
k	4.38×10^{14}	6.71×10^{-1}	4.33×10^{14}	6.64×10^{-1}	4.27×10^{14}	6.54×10^{-1}	4.40×10^{14}	6.74×10^{-1}	4.4×10^{14}	6.8×10^{-1}	4.41×10^{14}
l	7.51×10^{13}	1.16×10^{-1}	6.90×10^{13}	1.06×10^{-1}	7.34×10^{13}	1.13×10^{-1}	7.18×10^{13}	1.11×10^{-1}			5.49×10^{13}
m	3.38×10^{14}	2.57×10^{-1}	3.38×10^{14}	2.58×10^{-1}	3.36×10^{14}	2.56×10^{-1}	3.40×10^{14}	2.59×10^{-1}	3.4×10^{14}	2.6×10^{-1}	3.60×10^{14}
n	1.05×10^{13}	7.97×10^{-3}	9.08×10^{12}	6.88×10^{-3}	1.01×10^{13}	7.64×10^{-3}	9.76×10^{12}	7.39×10^{-3}			8.0×10^{12}
o	1.09×10^{13}	8.64×10^{-3}	1.02×10^{13}	8.07×10^{-3}	1.17×10^{13}	9.32×10^{-3}	1.09×10^{13}	8.62×10^{-3}			9.4×10^{12}
p	1.26×10^{13}	9.95×10^{-3}	1.23×10^{13}	9.70×10^{-3}	1.32×10^{13}	1.04×10^{-2}	1.24×10^{13}	9.77×10^{-3}			1.19×10^{13}
q	6.38×10^{14}	9.76×10^{-1}	6.27×10^{14}	9.59×10^{-1}	6.30×10^{14}	9.64×10^{-1}	6.40×10^{14}	9.79×10^{-1}			6.48×10^{14}
r	3.89×10^{14}	2.98×10^{-1}	3.80×10^{14}	2.92×10^{-1}	3.94×10^{14}	3.03×10^{-1}	3.94×10^{14}	3.02×10^{-1}	4.0×10^{14}	3.0×10^{-1}	3.48×10^{14}
s	2.20×10^{12}	3.35×10^{-3}	5.70×10^{10}	8.67×10^{-5}	5.60×10^{10}	8.52×10^{-5}	8.54×10^{10}	1.30×10^{-4}			2.9×10^{12}
t	2.74×10^{14}	2.09×10^{-1}	2.69×10^{14}	2.05×10^{-1}	2.59×10^{14}	1.97×10^{-1}	2.68×10^{14}	2.04×10^{-1}	2.7×10^{14}	2.0×10^{-1}	3.24×10^{14}
u	3.26×10^{13}	5.06×10^{-2}	3.25×10^{13}	5.04×10^{-2}	3.19×10^{13}	4.95×10^{-2}	3.11×10^{13}	4.82×10^{-2}			2.95×10^{13}
v	1.00×10^{13}	7.79×10^{-3}	9.81×10^{12}	7.62×10^{-3}	9.69×10^{12}	7.52×10^{-3}	9.36×10^{12}	7.27×10^{-3}			8.1×10^{12}

```
from pfac.atom import *
from pfac import fac
import os
asym = 'Ni'
os.system ('mkdir data')
nele = [1,2,3,4,5]
atomic_data(nele, asym, iprint = 1, dir ='data/')
```

Figure 5. FAC input written in Python language, used to generate atomic data for subsequent CRM simulations.

3. Collisional-Radiative Modelling

The CRM approach, implemented in the FAC code, is commonly used to model the spectral emission from plasmas. This theoretical framework determines the number of photons emitted from the plasma volume, which depends on two factors: (1) the photon spontaneous emission rate, which can be derived from pure atomic theory, and (2) the population of atoms in the upper (initial) state of radiative transition under specific plasma conditions, including electron temperature, electron density, and ion fractional abundance as a function of temperature.

In order to examine CRM implemented in FAC we tried to reproduce the experimental spectra from Bombarda et al. [3] work. CR modelling was performed in so-called three-ion model, in which radiative deexcitation, collisional excitation and ionization, radiative recombination and photoionization, resonance excitation, and dielectronic recombination processes are taken into account. The example of the FAC input as a Python file is presented in Figure 6. Two models of ionization equilibrium have been used: model 1 is based on default FAC-calculated ionization balances for Ni ions. Model 2 uses non-standard ionization balances (`FracAbund(z,temp,2,2)` parameters). As one can see from Figure 7, for model 1, the x, t, and $y + q$ peaks are underestimated. Model 2 reproduces very well the $y + q$ peak, and this model will be further used. More advanced improvement of CRM spectra requires manual changes of abundance of H-, Be-, and B-like Ni ions by some arbitrary factors [3]. The difference between `FracAbund(z,temp,2,2)` and default mode `FracAbund(z,temp)` (being equivalent of `FracAbund(z,temp,1,1)`) is described in detail in the FAC manual [29]. In practice, the `FracAbund(z,temp,2,2)` mode increases Ni^{25+}/Ni^{26+} and Ni^{24+}/Ni^{26+} abundance ratios compared to the numbers obtained with the `FracAbund(z,temp,1,1)` mode. As a consequence, for example, the q or β peaks are better modelled.

Figure 8 presents the X-ray spectra in the 1.585–1.620 Å wavelength range as a result of FAC CRM simulations for the He-like (Ni^{26+}) nickel ions and their dielectronic Li- (Ni^{25+}), Be- (Ni^{24+}), and B-like (Ni^{23+}) satellites for electron temperatures from 2 to 8 keV. The evolution of the shapes of Ni^{26+}, Ni^{25+}, Ni^{24+}, and Ni^{23+} ion spectra in particular are presented on Figures 9–12. The spectra were modelled as a sum of Gaussian profiles for each theoretical transition. The FWHM of these profiles was determined by thermal broadening (Γ_T) with the assumption that the electron temperature equals the ion temperature.

Using the theoretical shape of $n \geq 3$ satellites of Ni^{25+}, we determined the optimal profile for fitting these satellites in the experimental spectra. This profile is represented as a sum of three Gaussian components (see Figure 13), with their relative intensities and positions derived from the FAC simulations: $F = G(h_1, p_1, \Gamma) + G(h_2, p_2, \Gamma) + G(h_3, p_3, \Gamma)$, where $G(h, p, \Gamma)$ denotes a Gaussian function characterized by its height, position, and width. This approach has been used in our previous paper [4]. The obtained parameters are stored in Table 7. It is worth noting that although FAC CRM simulations consider 1350 transitions in the 1.5885–1.5920 Å range, only several of them are strong [4]. The 12 strongest lines (stronger than 3% of t line) account for 66% (CRM simulations for 8 keV electron tempera-

ture) through 70% (CRM simulations for 2 keV electron temperature) of the intensity of all satellites in the considered region. They are listed in Table 8.

```
from pfac.spm import *
from pfac import const
import~os

# Atomic number Z
z = 28

# Number of electrons
nele = 3

dir0 = 'data/'

# Temperature [eV]
temp = 3000

# Eelctron density [x 1.0$\times$10$^{10}$ cm-3]
den = 10000

dir1 = 'Ni%02d/'%nele
try:
   os.system('mkdir %s'%dir1)
except:
    pass

population=FracAbund(z,temp)
spectrum([nele], [temp], [den], [population], 'Ni',
         dir0 = dir0, dir1 = dir1, nion = 3)
```

Figure 6. Example of FAC input written in Python language, used to perform CRM simulations.

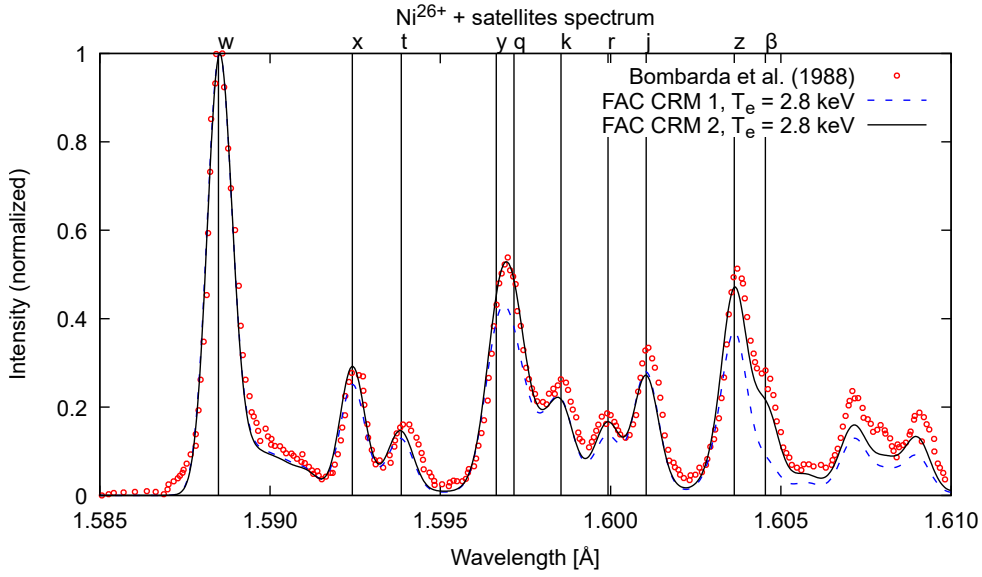

Figure 7. Recreated experimental spectrum from Bombarda et al. [3] (dots) compared to spectra simulated by FAC (dashed and solid lines).

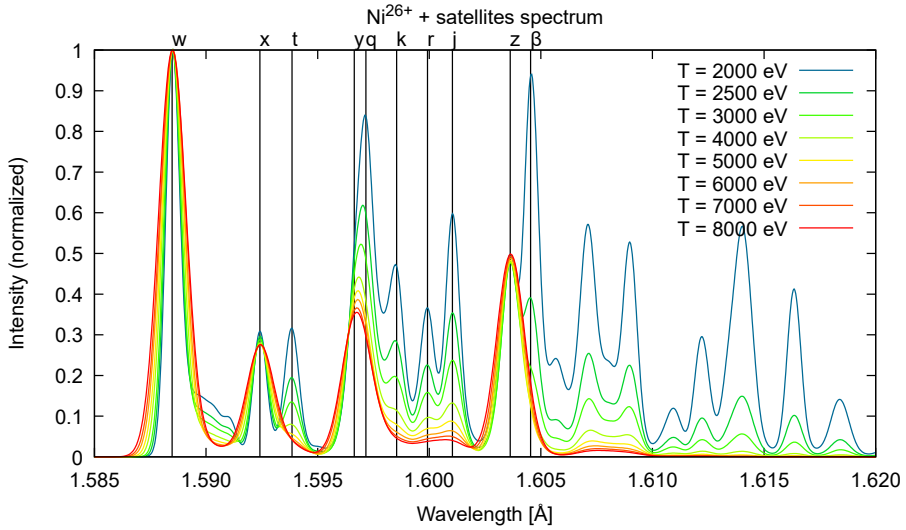

Figure 8. FAC CRM simulations for the X-ray spectra originating from the Ni^{26+}, Ni^{25+}, Ni^{24+}, and Ni^{23+} ions in the 1.585–1.620 Å wavelength range and 2–8 keV electron temperature range.

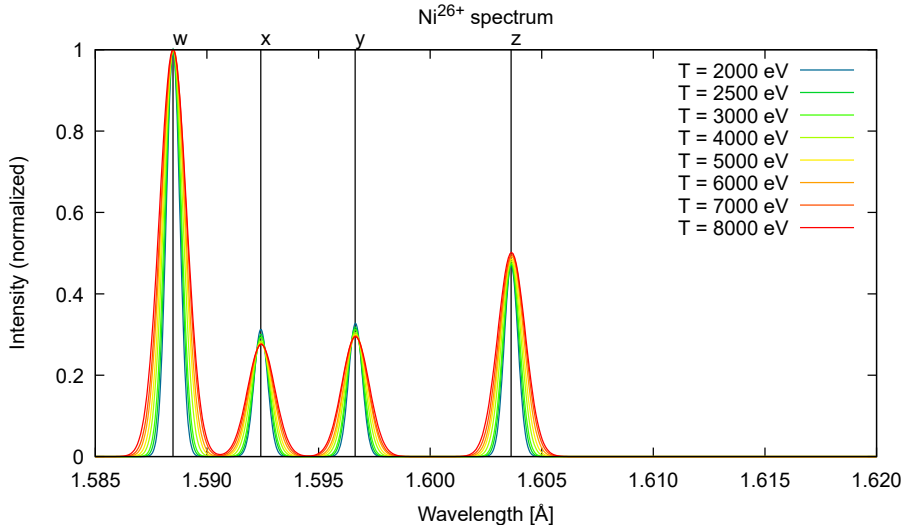

Figure 9. FAC CRM simulations for the X-ray spectra originating from the Ni^{26+} ions in the 1.585–1.620 Å wavelength range and 2–8 keV electron temperature range.

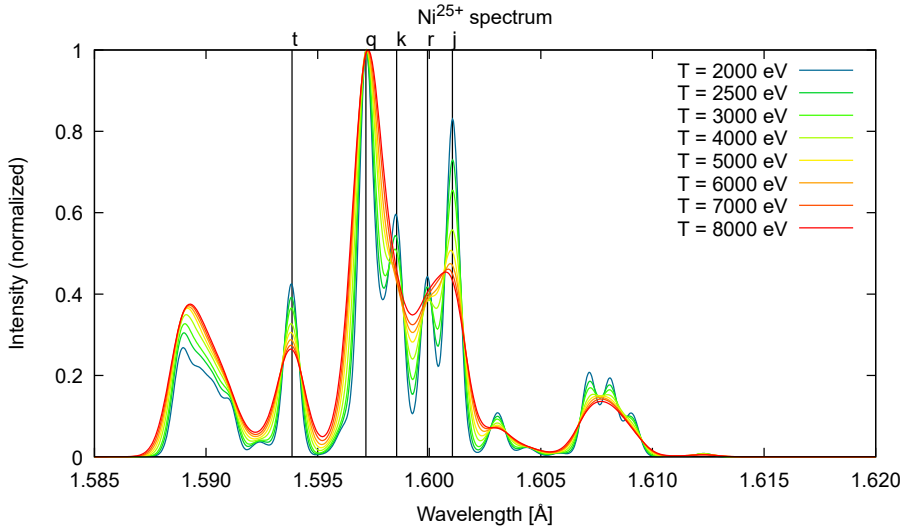

Figure 10. FAC CRM simulations for the X-ray spectra originating from the Ni^{25+} ions in the 1.585–1.599 Å wavelength range and 2–8 keV electron temperature range.

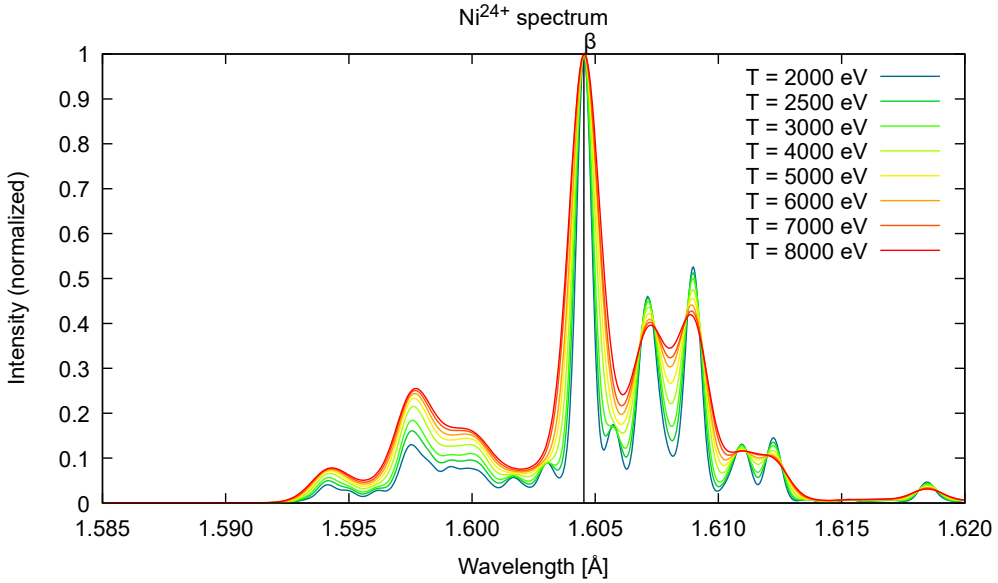

Figure 11. FAC CRM simulations for the X-ray spectra originating from the Ni^{24+} ions in the 1.585–1.620 Å wavelength range and 2–8 keV electron temperature range.

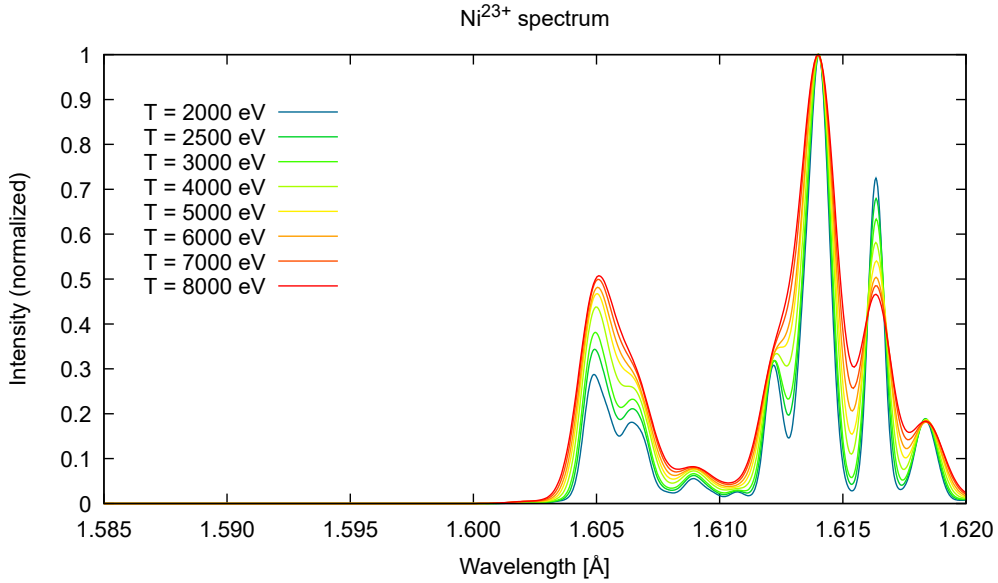

Figure 12. FAC CRM simulations for the X-ray spectra originating from the Ni^{23+} ions in the 1.585–1.599 Å wavelength range and 2–8 keV electron temperature range.

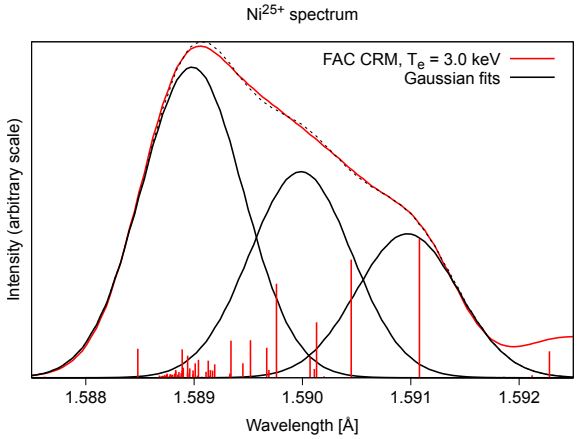

Figure 13. Approximation of the $n \geq 3$ satellites of Ni^{25+} lying in the range 1.588–1.592 Å by using three Gaussians.

Table 7. Parameter of the approximation of the $n \geq 3$ satellites of Ni^{25+} lying in the range 1.588–1.592 Å by using three Gaussians. Parameters h_1, h_2, and h_3 are the Gaussian profile heights for a given electron temperature (T) and for profile positions fixed at 1.58896 Å, 1.58996 Å, and 1.59094 Å, respectively. Γ denotes the Gaussian profile widths while Γ_T denotes the temperature broadening of a single transition.

T (keV)	Γ_T (Å)	h_1	h_2	h_3	Γ (Å)
2.0	7.15×10^{-4}	0.847	0.625	0.442	9.91×10^{-4}
2.2	7.50×10^{-4}	1.193	0.868	0.616	1.01×10^{-3}
2.4	7.84×10^{-4}	1.583	1.130	0.784	1.04×10^{-3}
2.6	8.16×10^{-4}	1.994	1.416	0.956	1.06×10^{-3}
2.8	8.47×10^{-4}	2.413	1.643	1.163	1.08×10^{-3}
3.0	8.76×10^{-4}	2.826	1.894	1.337	1.11×10^{-3}
3.2	9.05×10^{-4}	3.224	2.151	1.503	1.13×10^{-3}
3.4	9.33×10^{-4}	3.619	2.446	1.602	1.15×10^{-3}
3.6	9.60×10^{-4}	4.007	2.618	1.753	1.18×10^{-3}
3.8	9.86×10^{-4}	4.340	2.850	1.867	1.20×10^{-3}
4.0	1.01×10^{-3}	4.732	3.052	1.934	1.23×10^{-3}
4.2	1.04×10^{-3}	5.087	3.165	2.034	1.25×10^{-3}
4.4	1.06×10^{-3}	5.364	3.393	2.072	1.28×10^{-3}
4.6	1.09×10^{-3}	5.666	3.589	2.104	1.30×10^{-3}
4.8	1.11×10^{-3}	5.990	3.636	2.127	1.33×10^{-3}
5.0	1.13×10^{-3}	6.212	3.862	2.171	1.34×10^{-3}
6.0	1.24×10^{-3}	7.411	4.377	2.075	1.45×10^{-3}
7.0	1.34×10^{-3}	8.126	4.731	2.120	1.55×10^{-3}
8.0	1.43×10^{-3}	8.664	5.213	1.791	1.63×10^{-3}

Table 8. Strongest $n \geq 3$ satellites of Ni^{25+} in the 1.5885–1.5920 Å range. $P_{sat}(T)$ means the percentage of total satellite intensity for a given electron temperature.

Upper Level		Lower Level		Wavelength	Transition	$P_{sat}(T)$ (%)		
LSJ	jj	LSJ	jj	(Å)	Rate (s^{-1})	2 keV	4 keV	8 keV
$(1s\,2p\ ^1P)\ 3p\ ^2D_{5/2}$	$[(1s\,2p_{3/2})_1\ 3p_{3/2}]_{5/2}$	$1s^2\ 2p\ ^2P_{3/2}$	$[1s^2\ 2p_{3/2}]_{3/2}$	1.59108	5.76×10^{14}	16.1	15.0	14.4
$(1s\,2p\ ^1P)\ 3p\ ^2D_{3/2}$	$[(1s\,2p_{3/2})_1\ 3p_{1/2}]_{3/2}$	$1s^2\ 2p\ ^2P_{1/2}$	$[1s^2\ 2p_{1/2}]_{1/2}$	1.59045	5.38×10^{14}	13.7	12.8	12.3
$(1s\,2p\ ^1P)\ 3p\ ^2P_{3/2}$	$[(1s\,2p_{3/2})_1\ 3p_{3/2}]_{3/2}$	$1s^2\ 2p\ ^2P_{3/2}$	$[1s^2\ 2p_{3/2}]_{3/2}$	1.59013	5.27×10^{14}	6.4	6.0	5.8
$(1s\,2p\ ^1P)\ 3s\ ^2P_{1/2}$	$[(1s\,2p_{3/2})_1\ 3s]_{1/2}$	$1s^2\ 2s\ ^2S_{1/2}$	$[1s^2\ 2s]_{1/2}$	1.59007	5.27×10^{14}	2.5	2.3	2.2
$(1s\,2p\ ^1P)\ 3d\ ^2F_{7/2}$	$[(1s\,2p_{3/2})_1\ 3d_{5/2}]_{7/2}$	$1s^2\ 3d\ ^2D_{5/2}$	$[1s^2\ 3d_{5/2}]_{5/2}$	1.58976	5.01×10^{14}	10.9	10.2	9.8
$(1s\,2p\ ^1P)\ 4p\ ^2D_{5/2}$	$[(1s\,2p_{3/2})_1\ 4p_{3/2}]_{5/2}$	$1s^2\ 4p\ ^2P_{3/2}$	$[1s^2\ 4p_{3/2}]_{3/2}$	1.58967	6.05×10^{14}	3.2	3.4	3.4
$(1s\,2p\ ^1P)\ 4p\ ^2D_{3/2}$	$[(1s\,2p_{3/2})_1\ 4p_{1/2}]_{3/2}$	$1s^2\ 4p\ ^2P_{1/2}$	$[1s^2\ 4p_{1/2}]_{1/2}$	1.58952	5.93×10^{14}	4.0	4.2	4.3
$(1s\,2p\ ^1P)\ 4d\ ^2F_{7/2}$	$[(1s\,2p_{3/2})_1\ 4d_{5/2}]_{7/2}$	$1s^2\ 4d\ ^2D_{5/2}$	$[1s^2\ 4d_{5/2}]_{5/2}$	1.58934	6.07×10^{14}	4.0	4.2	4.3
$(1s\,2p\ ^1P)\ 5p\ ^2D_{3/2}$	$[(1s\,2p_{3/2})_1\ 5p_{1/2}]_{3/2}$	$1s^2\ 5p\ ^2P_{1/2}$	$[1s^2\ 5p_{1/2}]_{1/2}$	1.58913	6.00×10^{14}	1.8	2.0	2.0
$(1s\,2p\ ^1P)\ 5d\ ^2F_{7/2}$	$[(1s\,2p_{3/2})_1\ 5d_{5/2}]_{7/2}$	$1s^2\ 5d\ ^2D_{5/2}$	$[1s^2\ 5d_{5/2}]_{5/2}$	1.58904	6.08×10^{14}	1.9	2.1	2.1
$(1s\,2p\ ^1P)\ 3p\ ^2S_{1/2}$	$[(1s\,2p_{3/2})_1\ 3p_{3/2}]_{1/2}$	$1s^2\ 2p\ ^2P_{3/2}$	$[1s^2\ 2p_{3/2}]_{3/2}$	1.58894	4.12×10^{14}	2.6	2.4	2.3
$(1s\,2p\ ^1P)\ 3d\ ^2F_{5/2}$	$[(1s\,2p_{3/2})_1\ 3d_{5/2}]_{5/2}$	$1s^2\ 3d\ ^2D_{5/2}$	$[1s^2\ 3d_{5/2}]_{5/2}$	1.58889	2.42×10^{14}	3.3	3.1	3.0

4. Conclusions

In this study, we investigated the effect of electron correlation on the energies and rates of $L \rightarrow K$ transitions in He- and Li-like Ni ions, as well as the accuracy of collisional-radiative modelling simulations for such ions in plasma. Based on the findings presented, a few conclusions can be drawn:

(1) The influence of electron correlation on line ratios useful for plasma diagnostics is below 3%. This effect may have less impact on KX1 temperature diagnostics compared to other factors, such as the effect of toroidal plasma rotation shear [4].

(2) The quality of FAC CRM simulations can be improved by manipulating the ion balance model.

(3) The thousand-line region of $n \geq 3$ satellites of Ni^{25+} can be effectively approximated by a combination of three Gaussians, whose heights and widths depend on the plasma electron temperature.

Author Contributions: Conceptualization, K.K.; methodology, K.K.; formal analysis, K.K. and A.B.; investigation, K.K. and A.B.; writing—original draft preparation, K.K.; writing—review and editing, K.K., A.B. and J.R.; visualization, K.K.; supervision, J.R. All authors have read and agreed to the published version of the manuscript.

Funding: This work has been carried out within the framework of the EUROfusion Consortium and has received funding from the Euratom Research and Training Programme 2014–2020 under Grant Agreement No. 633053. The views and opinions expressed herein do not necessarily reflect those of the European Commission.

Data Availability Statement: The raw data supporting the conclusions of this article will be made available by the authors on request.

Conflicts of Interest: The authors declare no conflicts of interest.

References

1. Palmeri, P.; Quinet, P.; Mendoza, C.; Bautista, M.A.; García, J.; Witthoeft, M.C.; Kallman, T.R. Radiative and Auger Decay Data for Modeling Nickel K Lines. *Astrophys. J. Suppl. Ser.* **2008**, *179*, 542–552. [CrossRef]
2. Witthoeft, M.C.; Bautista, M.A.; García, J.; Kallman, T.R.; Mendoza, C.; Palmeri, P.; Quinet, P. K-shell photoionization of nickel ions using R-matrix. *Astrophys. J. Suppl. Ser.* **2011**, *196*, 7. [CrossRef]
3. Bombarda, F.; Giannella, R.; Källne, E.; Tallents, G.J.; Bely-Dubau, F.; Faucher, P.; Cornille, M.; Dubau, J.; Gabriel, A.H. Observations and comparisons with theory of the heliumlike and hydrogenlike resonance lines and satellites of nickel from the JET tokamak. *Phys. Rev. A* **1988**, *37*, 504–522. [CrossRef] [PubMed]
4. Kozioł, K.; Brosławski, A.; Patel, A.; Weisen, H.; Rzadkiewicz, J.; JET Contributors. Ion temperature spectroscopic measurements in high rotation discharges by means of X-ray diagnostic at JET. *J. Instrum.* **2022**, *17*, C07008. [CrossRef]
5. Czarnecka, A.; Zastrow, K.D.; Rzadkiewicz, J.; Coffey, I.H.; Lawson, K.D.; O'Mullane, M.G. Determination of metal impurity density, Δ Z eff and dilution on JET by VUV emission spectroscopy. *Plasma Phys. Control. Fusion* **2011**, *53*, 035009. [CrossRef]
6. Shen, Y.; Du, X.; Zhang, W.; Wang, Q.; Li, Y.; Fu, J.; Wang, F.; Xu, J.; Lu, B.; Shi, Y.; et al. Space-resolved extreme ultraviolet spectrometer system for impurity behavior research on experimental advanced superconducting Tokamak. *Nucl. Instrum. Methods Phys. Res. Sect. A Accel. Spectrometers Detect. Assoc. Equip.* **2013**, *700*, 86–90. [CrossRef]
7. Kubkowska, M.; Czarnecka, A.; Fornal, T.; Gruca, M.; Jabłoński, S.; Krawczyk, N.; Ryć, L.; Burhenn, R.; Buttenschön, B.; Geiger, B.; et al. Plasma impurities observed by a pulse height analysis diagnostic during the divertor campaign of the Wendelstein 7-X stellarator. *Rev. Sci. Instrum.* **2018**, *89*, 10F111. [CrossRef]
8. Bitter, M.; Hill, K.W.; Zarnstorff, M.; von Goeler, S.; Hulse, R.; Johnson, L.C.; Sauthoff, N.R.; Sesnic, S.; Young, K.M.; Tavernier, M.; et al. Satellite spectra for heliumlike titanium. II. *Phys. Rev. A* **1985**, *32*, 3011–3029. [CrossRef]
9. Hill, K.W.; Bitter, M.L.; Scott, S.D.; Ince-Cushman, A.; Reinke, M.; Rice, J.E.; Beiersdorfer, P.; Gu, M.F.; Lee, S.G.; Broennimann, C.; et al. A spatially resolving x-ray crystal spectrometer for measurement of ion-temperature and rotation-velocity profiles on the Alcator C-Mod tokamak. *Rev. Sci. Instruments* **2008**, *79*, 10E320. [CrossRef]
10. Bombarda, F.; Giannella, R.; Källne, E.; Tallents, G. Ion temperature measurement from doppler broadening of He-like nickel lines. *J. Quant. Spectrosc. Radiat. Transf.* **1989**, *41*, 323–333. [CrossRef]
11. Zastrow, K.; Morsi, H.W.; Danielsson, M.; von Hellermann, M.G.; Källne, E.; König, R.; Mandl, W.; Summers, H.P. Deduction of central plasma parameters from line-of-sight averaged spectroscopic observations. *J. Appl. Phys.* **1991**, *70*, 6732–6742. [CrossRef]
12. Eriksson, L.G.; Righi, E.; Zastrow, K.D. Toroidal rotation in ICRF-heated H-modes on JET. *Plasma Phys. Control. Fusion* **1997**, *39*, 27–42. [CrossRef]
13. Goryaev, F.; Vainshtein, L.; Urnov, A. Atomic Data for Doubly-Excited States 2lnl′ of He-like Ions and 1s2lnl′ of Li-like Ions with Z = 6–36 and n = 2, 3. *At. Data Nucl. Data Tables* **2017**, *113*, 117–257. [CrossRef]
14. Vainshtein, L.; Safronova, U. Wavelengths and transition probabilities of satellites to resonance lines of H- and He-like ions. *At. Data Nucl. Data Tables* **1978**, *21*, 49–68. [CrossRef]
15. Hata, J.; Grant, I.P. Wavelengths and radiative transition rates for selected lines of 2-, 3- and 4-electron systems for the elements from Ca to Cu. *Mon. Not. R. Astron. Soc.* **1984**, *211*, 549–557. [CrossRef]
16. Natarajan, L.; Kadrekar, R. Radiative decay from doubly and singly excited states of He-like nickel. *Phys. Rev. A- Opt. Phys.* **2013**, *88*, 012501. [CrossRef]
17. Sardar, S.; Wang, S.X.; Zhu, L.F. KLL Dielectronic Satellite Spectra from the Photorecombination of He-like Fe and Ni Ions. *Astrophys. J.* **2018**, *869*, 128. [CrossRef]
18. Chu, Y.; Ma, K. Transition energies and transition probabilities for the core-excited state (1s2s2p)3/2 of Li-like ions with Z = 6–92. *J. Electron Spectrosc. Relat. Phenom.* **2022**, *261*, 147264. [CrossRef]

19. Azarov, V.; Kramida, A.; Ralchenko, Y. A critical compilation of experimental data on the 1s2l2l′ core-excited states of Li-like ions from carbon to uranium. *At. Data Nucl. Data Tables* **2023**, *149*, 101548. [CrossRef]
20. Singh, G.; Singh, A.K.; Chowdhuri, M.B.; Nandi, T. Relativistic atomic structure calculations of Li-like ions used for plasma diagnostic studies. *Phys. Scr.* **2024**, *99*, 065408. [CrossRef]
21. Gabriel, A.H. Dielectronic Satellite Spectra for Highly-Charged Helium-Like Ion Lines. *Mon. Not. R. Astron. Soc.* **1972**, *160*, 99–119. [CrossRef]
22. Froese Fischer, C.; Gaigalas, G.; Jönsson, P.; Bieroń, J. GRASP2018—A Fortran 95 version of the General Relativistic Atomic Structure Package. *Comput. Phys. Commun.* **2019**, *237*, 184–187. [CrossRef]
23. Grant, I.P. *Relativistic Quantum Theory of Atoms and Molecules*; Springer Series on Atomic, Optical, and Plasma Physics; Springer: New York, NY, USA, 2007; Volume 40. [CrossRef]
24. Jönsson, P.; He, X.; Froese Fischer, C.; Grant, I.P. The grasp2K relativistic atomic structure package. *Comput. Phys. Commun.* **2007**, *177*, 597–622. [CrossRef]
25. Froese Fischer, C.; Godefroid, M.R.; Brage, T.; Jönsson, P.; Gaigalas, G. Advanced multiconfiguration methods for complex atoms: I. Energies and wave functions. *J. Phys. B At. Mol. Opt. Phys.* **2016**, *49*, 182004. [CrossRef]
26. Kozioł, K.; Rzadkiewicz, J. Multiconfiguration Dirac-Hartree-Fock and configuration-interaction study of 4d–3p x-ray transitions in Cu- and Ni-like tungsten ions. *Phys. Rev. A* **2018**, *98*, 062504. [CrossRef]
27. Gu, M.F. The flexible atomic code. *Can. J. Phys.* **2008**, *86*, 675–689. [CrossRef]
28. Kramida, A.E.; Ralchenko, Y.; Reader, J.; Team, N.A. *NIST Atomic Spectra Database*; Version 5.12; National Institute of Standards and Technology: Gaithersburg, MD, USA, 2024. Available online: https://physics.nist.gov/asd (accessed on 5 December 2024). [CrossRef]
29. Gu, M.F. FAC Manual. Available online: https://github.com/flexible-atomic-code/fac (accessed on 6 February 2025).

Disclaimer/Publisher's Note: The statements, opinions and data contained in all publications are solely those of the individual author(s) and contributor(s) and not of MDPI and/or the editor(s). MDPI and/or the editor(s) disclaim responsibility for any injury to people or property resulting from any ideas, methods, instructions or products referred to in the content.